Materials Advances

PAPER

View Article Online
View Journal | View Issue

Check for updates

Cite this: *Mater. Adv.*, 2024, 5, 5307

Hydrothermal synthesis of an MoS_2/MnO_2 nanocomposite: a unique 3D-nanoflower/1D-nanorod structure for high-performance energy storage applications†

Md. Roxy Islam,[a] Mizanur Rahaman,[b] Md. Muktadir Billah*[a] and Muhammad Rakibul Islam *[b]

Received 23rd January 2024,
Accepted 29th April 2024

DOI: 10.1039/d4ma00065j

rsc.li/materials-advances

In this study, an MoS_2/MnO_2 nanocomposite electrode with a novel 3D nanoflower/1D nanorod architecture is effectively synthesized using a straightforward, cost-effective hydrothermal process. The addition of the 1D MnO_2 nanorod offers a structural backbone, while the 3D MoS_2 nanoflower generates additional reactive active sites. The hybrid structure makes fast electron and ion movement possible, which also increases the capacity for charge collection. This leads to 199.12 F g^{-1} specific capacitance at 40 mA g^{-1} in a designed 3D-1D MoS_2/MnO_2(6 wt%) electrode and exceptional rate capability with a tremendous cycling life (95% capacitance retention after 10 000 cycles). This discovery paves the way for the low-cost and straightforward construction of a hierarchical nanocomposite electrode with improved charge storage and electrical conductivity in energy storage applications like supercapacitors.

1. Introduction

Energy from renewable sources is becoming a major topic due to the fast expansion of the world economy, rapid consumption of fossil fuels, and global climate change. Using renewable energy sources, such as wind, water, sun, and others, is a path to reduce current pollution and energy problems.[1–4] However, a continuous energy supply from renewable sources is not accessible due to the unavailability of sunlight throughout the entire time period and the unreliability of wind and tides. An alternative way to maintain a sustainable energy future by using energy from renewable sources is to use advanced energy storage devices, such as fuel cells, batteries, and supercapacitors (SCs).[1,5–9] Among the available energy storage alternatives, SCs are now in the limelight because of their low price, longer cycle life, high density of energy, *etc.* and are suitable for applications that require rapid and higher-power energy.[10–12] Because of their increased power density, safety, benefits of high charge–discharge rate, outstanding cycle stability, extended cycle life, low-temperature operation, low maintenance cost, *etc.*, supercapacitors may replace batteries thus piquing the scientific and technological attention of many.[11,13–18] For such advantages, SCs find their applications in smart door locks, hybrid forklifts, cranes, smart grids, televisions, UPS (uninterruptible power supply) systems, electric vehicles, and other electronic devices.[19,20]

A transition metal dichalcogenide called molybdenum disulfide (MoS_2) can be employed as an active component for designing energy storage devices, due to its electrical conductivity, surface area, and intrinsic ion conductivity which suggests good electrochemical properties.[21–25] The two-dimensional planar layered structure of MoS_2 is interconnected with sulfur–molybdenum–sulfur bonds. Mo atoms have different valence states (+2 to +6) and the interlayered space conducive to the electrolytic cation intercalation gives MoS_2 electrochemically pseudo-capacitance properties. But MoS_2 has moderate interfacial active sites to react with electrolyte ions, poor cycling stability, low energy density, and no stability in the interphase layer of electrolyte–solid, and it shows structural destruction especially aggregation during charge/discharge cycles, which are the drawbacks for supercapacitors.[26–28]

Metal oxide nanoparticles such as Co_3O_4, NiO, V_2O_5, TiO_2, and MnO_2 have been added to the MoS_2 structure to enhance its capacitive properties.[29–35] Kanaujiya *et al.*[29] synthesized mesoporous MnO_2@MoS_2 nanocomposites using a versatile hydrothermal approach. Wang *et al.*[32] have synthesized hierarchical MoS_2/Mn_3O_4 hybrid architectures where nanoparticles of Mn_3O_4 are uniformly incorporated into MoS_2 thin layers and achieved two times more capacitance than MoS_2 with 69.3% capacitance retention. Liao *et al.*[33] fabricated a MoS_2/MnO_2

---

[a] *Department of Materials and Metallurgical Engineering, Bangladesh University of Engineering and Technology, Dhaka, Bangladesh. E-mail: mbillah@mme.buet.ac.bd*

[b] *Department of Physics, Bangladesh University of Engineering and Technology, Dhaka, Bangladesh. E-mail: rakibul@phy.but.ac.bd*

† Electronic supplementary information (ESI) available. See DOI: https://doi.org/10.1039/d4ma00065j

(nanosheet/nanowire) hybrid using the lithography technique to analyze the interfacial impact on the storage of energy. But, MoS_2 nanosheet preparation methods take time and the yield is low. Those nanosheets have a restacking tendency at the time of charging–discharging that produces high surface energy and as a result, the electrical conductivity reduces.[36–40] To solve those drawbacks, a cost-effective procedure providing a higher yield, for example, a simple hydrothermal synthesis route, can play a vital role in producing a flower-like 3D-MoS_2 nanostructure. The MoS_2 nanoflower can give a high specific surface area, where a lot of interfacial active sites are present to react with electrolyte ions.[29] Due to the presence of a larger surface area and greater electrolytic ion migration active spots, the flower-shaped nanostructure has the ability to store more energy. Moreover, a longer cycle life can be maintained when it is used as the active material of electrodes.[41] Additionally, the incorporation of nanoparticles into the flower-shaped structure may generate an increased number of active spots for the electrolytic ion diffusion, greater stability of the structure, and defect-rich surface.[42–45] However, as far as we know, the electrochemical behavior of nanocomposites made of a 3D MoS_2 nanoflower (NF) and 1D MnO_2 nanorods produced with various MoS_2 and MnO_2 weight ratios has not been thoroughly investigated.

In this study, an MoS_2 nanoflower/MnO_2 nanorod, a distinctive structurally combined nanocomposite, has been prepared to improve the capacitive performance of an MoS_2 nanoflower. Here, a hydrothermal method has been used to prepare MoS_2 nanoflowers and MnO_2 nanorods and to incorporate the rod-shaped MnO_2 nanoparticles into the MoS_2 nanoflowers in varying concentrations (2, 4, and 6 wt%). Manganese oxide (MnO_2) is a metal oxide semiconductor and has its own high theoretical capacitance, nontoxic nature, high cycling stability, electro-catalytic activity, lower cost, and abundance advantages.[46,47] MnO_2 has different polymorphs, and among them, our synthesized MnO_2 contains double chains of edge-sharing MnO_6 octahedral which exhibits high catalytic activities.[48] The addition of MnO_2 nanorods into MoS_2 nanoflowers may give more stability to the structure, rapid transportation of ions, and effective surface interactions with electrolyte ions; therefore, cycling stability and capacitance of MoS_2 nanoflowers may increase.[45]

In this experiment, the physical and structural characteristics of synthesized samples were studied by FE-SEM (field emission scanning electron microscopy), HR-TEM (high-resolution transmission electron microscopy), and XRD (X-ray diffraction), respectively. FE-SEM results show that the as-synthesized MnO_2 has a 1D nanorod structure. The synthesized MoS_2/MnO_2 nanocomposites and pure MoS_2 have a 3D flower-shape morphology consisting of many nanolayered petals. HR-TEM results show that MnO_2 nanorods are present between the MoS_2 nanosheets in MoS_2/MnO_2 nanocomposites, and the interlayer spacing of MoS_2 increases with the MnO_2 concentration. XRD analysis reveals that the crystallite size decreases and the dislocation density increases for the MoS_2 NF when increased amounts of MnO_2 nanorod are added. Using a system of three electrodes, the electrochemical behavior of the as-synthesized samples was examined in 0.5 M Na_2SO_4 electrolyte at room temperature. Among all synthesized MoS_2/MnO_2 nanocomposites (NCs), MoS_2/MnO_2 (6 wt%) NC can store 199.12 F g^{-1} at a 40 mA g^{-1} current density. Here the density of energy was found to be 6.91 W h kg^{-1} at a 10 W kg^{-1} power density. At 170 mA g^{-1} current density, the MoS_2/MnO_2 (6 wt%) NC undergoes 10 000 charge/discharge cycles and provides 95% capacitance retention which confirms its tremendous cycling stability. The MoS_2/MnO_2 nanocomposites show a higher capacitance than the bare MoS_2 electrode denoting that the 3D MoS_2 nanoflower incorporated with the MnO_2 nanorod gives a larger specific surface area, greater interlayer spacing, higher wettability, faster intrinsic electrical conductivity, improved electrolytic cation intercalation at the interface, and an overall defect-rich structure. The novelty of this work is the synthesis of 3D-nanoflower/1D-nanorod structural nanocomposites of MoS_2/MnO_2, and when compared (Table 5) to the capacitance of MoS_2 based supercapacitors that have been published in the different literature, our synthesized MoS_2/MnO_2 (6 wt%) NC shows good capacitance alongside capacitance retention. So, to prepare a high-performance energy storage device, this experiment can provide significant insights.

2. Section of experimentation

2.1. Chemical reagents

Sodium molybdate dihydrate ($Na_2MoO_4·2H_2O$), manganese sulfate monohydrate ($MnSO_4·H_2O$), potassium permanganate ($KMnO_4$), and dimethyl sulfoxide (C_2H_6OS) were obtained from Merck, Darmstadt, Germany. From Research Lab, India, thiourea (CH_4N_2S), sodium sulfate (Na_2SO_4) and polyvinyl alcohol (PVA) $(C_2H_4O)_x$ were collected. Without any purification, analytical grade chemicals were used.

2.2. MoS_2 NF preparation

A clear precursor solution was prepared by dissolving 0.14 M sodium molybdate dihydrate and 0.65 M thiourea in 120 ml of deionized water. Then the solution was kept in a Teflon-lined autoclave for 24 hours at 200 °C. The resultant black precipitate was then collected from the autoclave and after drying at 70 °C for several hours the MoS_2 nanoflower was obtained.

2.3. MnO_2 nanorod preparation

5.6878 g of $MnSO_4·H_2O$ and 2.3657 g of $KMnO_4$ were taken in 140 mL of deionized water. After stirring for 30 minutes, the solution was kept in a Teflon-lined autoclave for 12 h in an oven at 140°. After collecting the resultant brown precipitate, it was dried for a few hours at 80 °C yielding the MnO_2 nanorod.

2.4. Preparation of the MnO_2 incorporated MoS_2NF

Fig. 1(a) shows the schematic representation of nanocomposite preparation. At first, a desired amount of MnO_2 nanorod was added to 50 mL of deionized water and sonicated for 1 hour. After dissolving 0.14 M sodium molybdate dihydrate and 0.65 M thiourea in 70 mL of deionized water, the solution

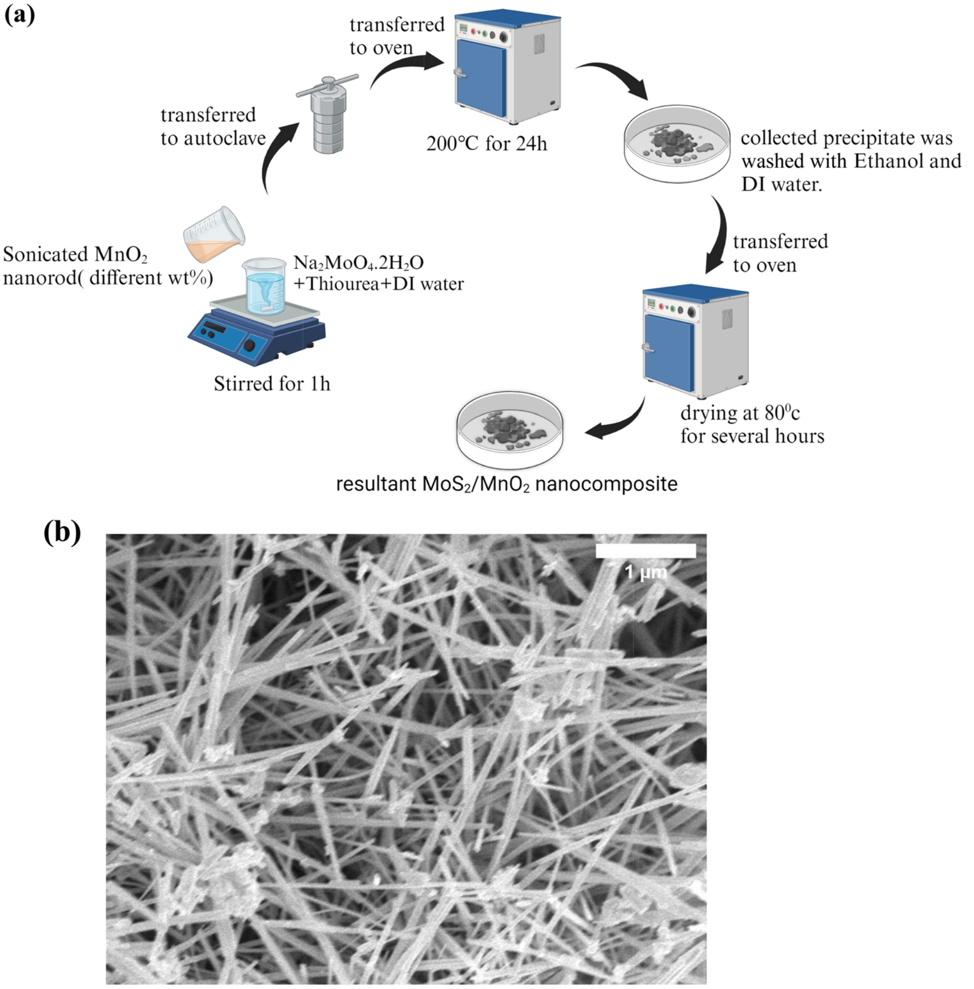

Fig. 1 (a) Schematic representation of the synthesis of MoS_2/MnO_2 nanocomposites. (b) FE-SEM image of the MnO_2 nanorod at a low magnification.

was transferred to the sonicated 50 mL MnO_2 solution. After stirring for 1 hour, the whole solution was kept in a Teflon-lined autoclave for 24 h at 200 °C. The desired black precipitate was collected and dried for a few hours at 80 °C. Various amounts of MnO_2 nanorods such as 2 wt%, 4 wt%, and 6 wt% were incorporated. The NCs are entitled as MoS_2/MnO_2 (2 wt%), MoS_2/MnO_2 (4 wt%) and MoS_2/MnO_2 (6 wt%) respectively.

2.5. Preparation of electrodes

To prepare working electrodes, a 100 μL slurry of the as-synthesized material was deposited on a cross-sectional surface (0.3 cm^2) of a modified graphite electrode. To prepare the slurry, PVA (4% of the as-synthesized material) and dimethyl sulfoxide were added to the as-synthesized material. After sonicating for 1 h, the slurry was deposited and for drying, the working electrodes were kept at 70 °C. Here PVA acts as a binder and dimethyl sulfoxide works as a polar aprotic solvent.[49,50]

2.6. Characterization

To get the microscopic information about the surface of the as-synthesized samples, FE-SEM (JSM 7600, Jeol) images were taken. Microstructural and morphological properties of the synthesized materials were also observed using HR-TEM (JEOL, JEM 2100 F) images. Using the radiation of CuK_α (λ = 1.5406 Å) of the X-ray diffractometer of 3040XPert PRO, Philips, the XRD data were obtained. The electrochemical capabilities of the as-synthesized samples were investigated by using a CS310 electrochemical workstation (Corrtest, China) in 0.5 M Na_2SO_4 electrolyte using a three-electrode system. Here the working electrode is a modified graphite electrode, the reference electrode is Ag/AgCl, and the counter electrode is a platinum plate (1 cm × 1 cm).

3. Results and discussion

3.1. Scanning electron microscopy

Fig. 1(b) presents the FESEM image of MnO_2 consisting of densely aligned disorderly arranged nanorods with several micrometers of length and a width of 47–98 nm. Some fragmented nanorods were observed and the formation of bundled nanorods could be seen. Under high magnification (Fig. S1, ESI†), the surface of the nanorods appears to be smooth.[45,51]

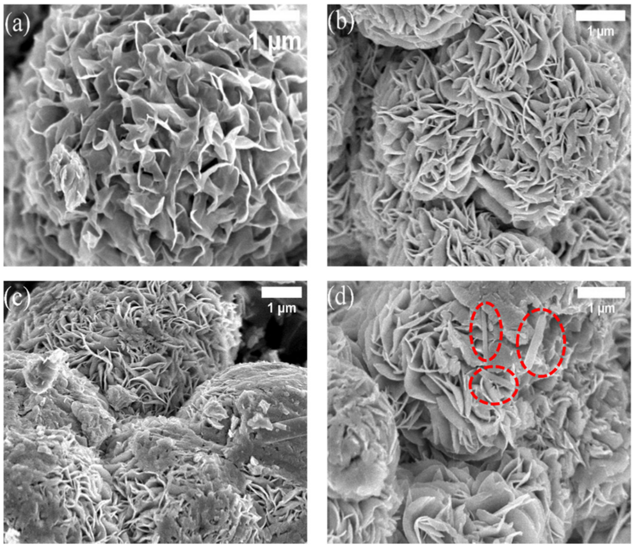

Fig. 2 (a)–(d) FE-SEM images of MoS_2 NF, MoS_2/MnO_2 (2 wt%), MoS_2/MnO_2(4 wt%), and MoS_2/MnO_2 (6 wt%) nanocomposites, respectively.

From the FESEM image of MoS_2 (Fig. 2(a)), flower-like spherical 3D nanostructures were observed that confirm the successful synthesis of MoS_2 nanoflowers having a diameter between 5 and 6 μm. Those nanoflowers consist of plenty of aligned curved petals, which are assembled by several MoS_2 nanosheets, through a common inner center. The petal thickness is observed to be varied between 2 and 5 nm.[52] Fig. 2(b–d) shows FESEM images of MoS_2/MnO_2 nanocomposites for different concentrations of MnO_2, where the curved petals of MoS_2 are more uniform and smoothly aligned. These nanoflowers with observed diameters in the range of 4–6 μm are in the cluster form or not dependent on each other.[53] When the MnO_2 nanorod was taken in the precursor solution of MoS_2, Mo^{4+} ions from the cationic precursor could be attracted on the surface of the MnO_2 nanorod because of van der Waals, cohesive or electrostatic, or other chemical forces.[45] S^{2-} ions from the anionic precursor combine with Mo^{4+} ions on the surface of the MnO_2 nanorod to form flower-shaped nanostructures.

From Fig. 2(b–d) we observe that the diameter of the MoS_2 nanoflower reduces with the addition of MnO_2 and the thickness of the petal for MoS_2/MnO_2(2 wt%) is in the range of 10–20 nm but for MoS_2/MnO_2(4 wt%) and MoS_2/MnO_2(6 wt%), the thickness got increased (20–40 nm) may be due to agglomeration of multiple layers of nanosheets.[54] Due to the increase of petal thickness, porosity and specific surface area would increase and as a result more electrical contact with the current collector would provide an excellent charge transfer rate and improvement in electrochemical capacity. As shown in Fig. 2(b and c), the existence of MnO_2 nanorods is not clearly observed which may be due to the low concentration of MnO_2. For higher concentrations of MnO_2, nanorods are clearly observed as shown in Fig. 2(d).

From EDX mapping shown in Fig. S2(a–d) (ESI†), the compositional information shown in Table 1 reveals that the surface of the MoS_2 NF is enriched with S atoms. In addition, in Fig. 2(b–d) the presence of dispersed fragmented particles on the surface of petals with Mo, S, Mn, and O elemental distribution from EDX mapping confirms that the petals consist of Mo and S and the fragmented particle has Mn and O. From the EDX results, we observe that the %atomic ratio of S and Mo was greater than 4, and this excess amount of sulfur atoms appeared as a result of many defects on the ultrathin MoS_2 nanosheets. The defective structures can provide more stability to the nanosheets by reducing the surface energy and generating more reactive sites.[55,56]

3.2. Transmission electron microscopy

TEM images of MoS_2 NF and MoS_2/MnO_2 nanocomposites are shown in Fig. 3(a–d). From Fig. 3(a) it can be observed that the MoS_2 NF consists of many thin petals and those petals are composed of several MoS_2 nanosheets. As shown in Fig. 3(b–d), the curved and wrinkled nanosheets of MoS_2 are very thin and partially transparent. Light contrasts in various areas indicate the ultra-thin nature of the nanosheets. In the TEM image (Fig. 3(b–d)) of MoS_2/MnO_2(2, 4, 6 wt%) nanocomposites, the presence of MnO_2 nanorods between MoS_2 nanosheets is clearly visible. The transfer of electrons between MoS_2 and MnO_2 is facilitated due to the close integration between MnO_2 and MoS_2. Fig. 4(a–d) displays HR-TEM images along with the associated SAED (selected area electron diffraction) patterns. From the HRTEM image, in Fig. 4(a), we observed disorderly arranged lattice fringes and weak diffraction rings as shown in the inset SAED pattern confirming the poor crystallinity of the MoS_2 NF.[57]

The magnified HRTEM image (Fig. 4(a)) provides an interlayer spacing of 0.63 nm that agrees with the hexagonal MoS_2 (002) plane indicating the growth of hexagonal nanosheets along the vertical [002] crystal axis.[58] The interlayer spacings for MoS_2/MnO_2(2 wt%), MoS_2/MnO_2(4 wt%), and MoS_2/MnO_2(6 wt%) were found to be 0.64 nm, 0.65 nm, and 0.67 nm, respectively indicating a lattice expansion due to the addition of MnO_2.[28] Such an increase of interlayer spacing may be attributed to the diffusion of MnO_2 between MoS_2 layers.[59] The enlargement

Table 1 Elemental analysis from EDX mapping

MnO_2 concentration (wt%) in the prepared samples	Mo (atom%)	S (atom%)	Mn (atom%)	O (atom%)	Mo : S
0	6.62	93.38	0	0	1 : 14
2	11.82	70.30	0.63	17.25	1 : 6
4	8.34	63.74	0.78	27.09	1 : 7
6	8.64	77.29	0.98	13.09	1 : 9

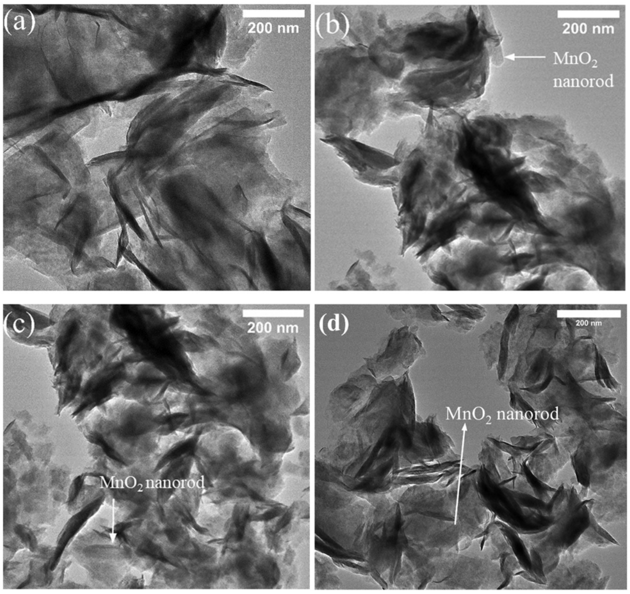

Fig. 3 (a)–(d) TEM images of MoS_2 NF, MoS_2/MnO_2 (2 wt%), MoS_2/MnO_2 (4 wt%) and MoS_2/MnO_2 (6 wt%) nanocomposites, respectively.

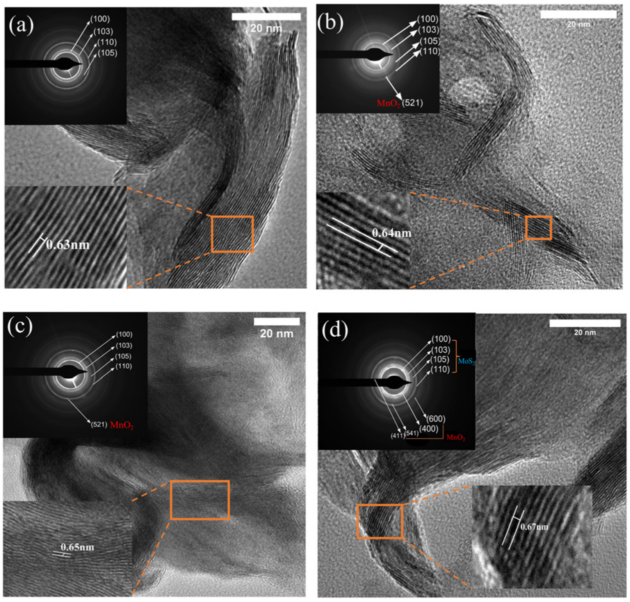

Fig. 4 (a)–(d) HR-TEM images of MoS_2 NF, MoS_2/MnO_2 (2 wt%), MoS_2/MnO_2 (4 wt%), and MoS_2/MnO_2 (6 wt%) nanocomposites, respectively. The insets of figures (a)–(d) show the corresponding SAED patterns.

of interlayer spacing and unique nanoflower-nanorod morphology may provide better ions intercalation, more electroactive sites, and enhancement of electrolyte access that gives the desired electrochemical property with improved efficiency in attaining higher capacitance.[29,45,59]

The SAED patterns for all the samples (inset of Fig. 4(a–d)) show bright concentric rings of diffraction that ensure the polycrystalline nature of the as-synthesized samples. Also, diffraction rings (inset of Fig. 4(a–d)) of the (100), (103), (105), and (110) lattice planes of MoS_2 are observed in all as-synthesized samples. Due to the low concentration of MnO_2, only lattice plane (521) is observed in (inset of Fig. 4(b and c)) MoS_2/MnO_2 (2 wt%) and MoS_2/MnO_2 (4 wt%). When the concentration of MnO_2 is increased, (400), (411), (541), and (600) lattice planes of MnO_2 nanorods are found in MoS_2/MnO_2 (6 wt%) nanocomposites.

The findings from the TEM analysis demonstrate that the MoS_2/MnO_2 nanocomposites were successfully prepared and confirm intimate contact between the MnO_2 nanorods and the MoS_2 NF. From the TEM images of the nanocomposite, discontinuity in the lattice fringes of the curled edges suggests that the crystals possess dislocations and defects.[53,56]

3.3. X-ray diffraction

The XRD patterns were studied to confirm the phase, structure, and crystallinity of the MoS_2 nanoflower and MoS_2/MnO_2 nanocomposites, as shown in Fig. 5. As illustrated in Fig. 5(a), the hexagonal phase of MoS_2 (JCPDS No. 37-1492), which is a member of the space group *P*63/*mmc*, agrees well with the diffraction peaks of the pristine MoS_2. The peaks at $2\theta = 14.04^\circ$, 33.49°, 39.46°, 48.57°, and 59.14° are attributed to the (002), (100), (103), (105) and (110) lattice planes, respectively.[53] Each reflection in the XRD pattern seen in Fig. S3 (ESI†) for the MnO_2 nanorod may easily be attributed to a pure tetragonal phase of the space group *I*4/*m* (no. 87), with $a = 0.985$ nm and $c = 0.285$ nm (for the lattice constants). The absence of peaks for any other manganese oxides

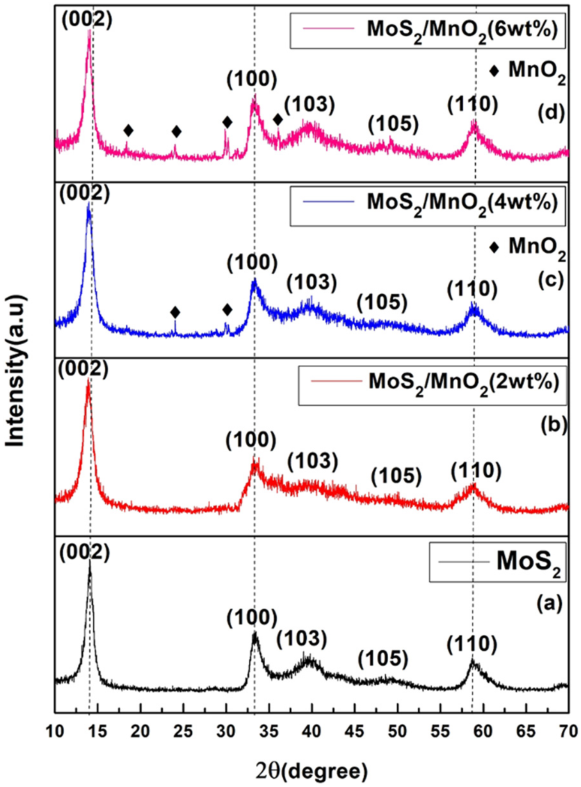

Fig. 5 XRD patterns of pure MoS_2 NF and synthesized nanocomposites of MoS_2/MnO_2.

suggests that the produced MnO_2 nanorods have a pure phase.[60] In Fig. 5(a) the sharp peak of pure MoS_2 nanoflower at 14.04°, which has a 0.63 nm *d*-spacing corresponding to the (002) plane, confirms that MoS_2 layers stacked toward the c axis during synthesis.[61]

For MoS_2/MnO_2 nanocomposites, all the primary diffraction peaks of pure MoS_2 are present. Due to the low concentration of MnO_2 in MoS_2/MnO_2 (2 wt%), no diffraction peak of MnO_2 is observed. But the primary characteristic peaks of MnO_2 can be only clearly observed for MoS_2/MnO_2(4 wt%) and MoS_2/MnO_2(6 wt%) nanocomposites.[44,62,63] For MoS_2/MnO_2 NCs the broadened and weak diffraction of the (002) plane imply low crystallinity, indicating that the pristine MoS_2 NF has a larger average crystallite size than that of the MoS_2/MnO_2 nanocomposites.[64] A lower angle shift of the initial XRD peak occurs, which may be due to lattice distortion, indicating an increase in the MoS_2 interlayer distance in the nanocomposites.[64,65]

The crystallite size (L), the density of dislocation (δ), and the microstrain (ε) of all samples were determined from the (002) peak using eqn (1)–(3), respectively.[66,67]

$$L = \frac{0.94\lambda}{\beta\cos\theta}. \tag{1}$$

$$\delta = 1/L^2 \tag{2}$$

$$\varepsilon = \frac{\beta}{4\tan\theta}. \tag{3}$$

where λ = X-ray wavelength, θ = diffraction angle, and β = diffraction peak's FWHM (full width at half-maximum).

At the (002) peak, the structural parameters were measured. Table 2 and Fig. 6 present the variation of structural parameters of the MoS_2 NF and MoS_2/MnO_2 NCs.[68–70] The crystallite size was found to be decreased from 7.51 nm to 5.59 nm when the concentration of MnO_2 increased from 2 wt% to 6 wt%.[68–70] Because the presence of MnO_2 nanorods helps to grow cross-linked MoS_2 nanosheets.[71,72] Microstrain and dislocation density increase with the concentration of MnO_2 suggesting increased defect states like dislocation generation, imperfect crystal structure, and vacancies in the MoS_2 NF.[73,74] Using the following equations, the values of lattice constants were calculated:

$$\frac{1}{d^2} = \frac{4}{3}\frac{h^2+hk+k^2}{a^2} + \frac{l^2}{c^2}$$

$$d = \frac{\lambda}{2\sin\theta}$$

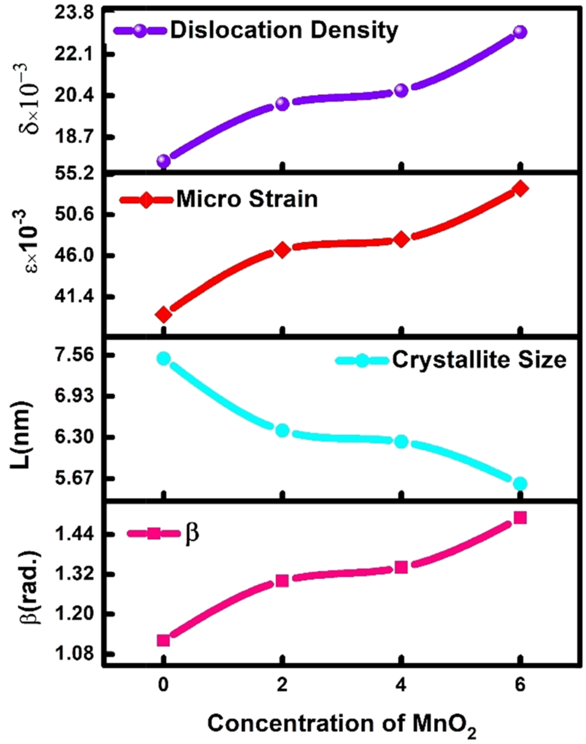

Fig. 6 The variation of several X-ray diffraction parameters for different wt% of MnO_2.

where a, b, and c denote lattice constants, d = atomic plane spacing, λ = wavelength (1.5406 Å), (h, k, l) denotes miller indices, and θ = incident angle. The calculated values (in Table 1) of lattice constants are less than standard values which represent less volume of lattice cell.[75] Increased dislocation density, smaller crystallite size, and difference in d spacing create lattice distortion. As a result, defects in lattice occur which gives profound active sites with an improved surface area, and at the time of charging/discharging, the charge transfer rate increases between active materials and solution.[76–79]

3.4. Electrochemical performance analysis

3.4.1. Cyclic voltammetry. The cyclic voltammetry (CV) plots of the MoS_2 NF and MoS_2/MnO_2 NCs were analyzed with the applied potential between −0.3 and 0.2 V at the scan rates of 5, 10, 20, 30, 40, 50, and 70 mV s^{-1} as shown in Fig. 7(a–d). For all the samples quasi-rectangular shapes of CV curves without any redox peaks were observed. The area for the CV plots of MoS_2/MnO_2 nanocomposites is larger than that of MoS_2 NF indicating an increase in capacitance due to the incorporation of MnO_2.

Table 2 XRD study revealed the diffraction parameters for pristine MoS_2 NF and MoS_2/MnO_2 NCs

Synthesized particles	β (radian)	L (nm)	d (Å) (002)	d (Å) (100)	$a = b$ (Å)	c (Å)	$\varepsilon \times 10^{-3}$	$\delta \times 10^{-3}$ (nm^{-2})
MoS_2	1.12	7.51	6.30	2.672	3.08	12.60	39.41	17.71
MoS_2/MnO_2(2 wt%)	1.30	6.40	6.35	2.675	3.09	12.70	46.65	20.07
MoS_2/MnO_2(4 wt%)	1.34	6.23	6.34	2.671	3.08	12.68	47.85	20.61
MoS_2/MnO_2(6 wt%)	1.49	5.59	6.37	2.674	3.09	12.75	53.58	23.01

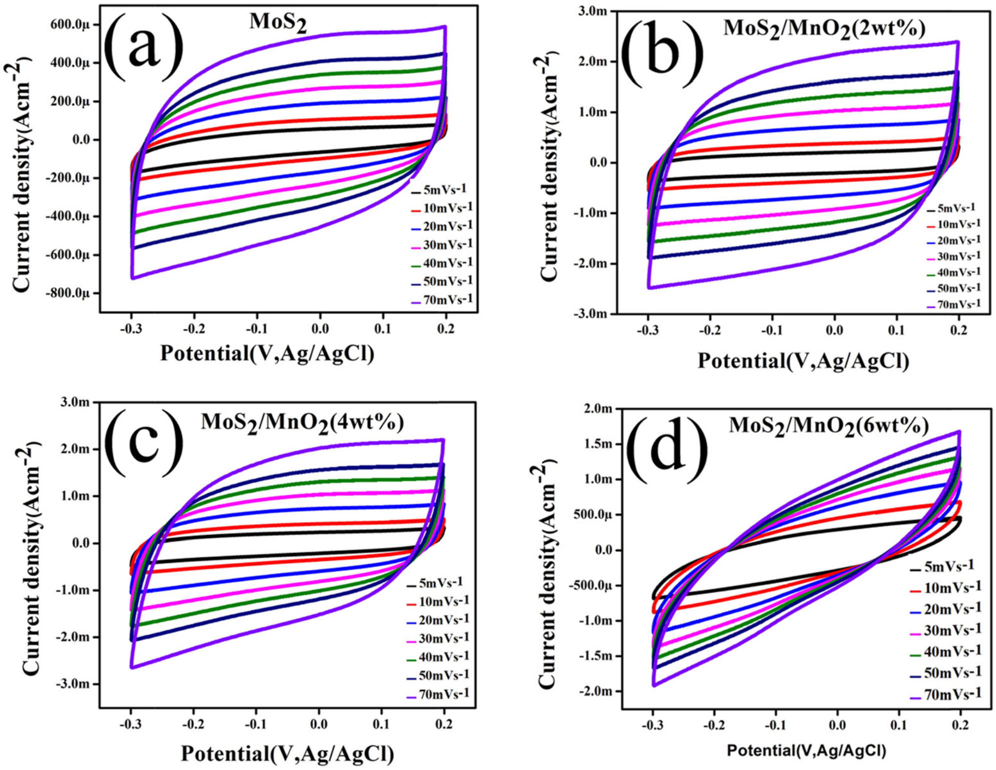

Fig. 7 (a)–(d) CV plots of pure MoS_2 NF and MoS_2/MnO_2 NCs at various scan rates.

Na^+ cation has a great impact on the charge–discharge electrochemistry of the MoS_2 NF and MoS_2/MnO_2 nanocomposites. A mechanism could be suggested as follows:[57,80–83]

$$MoS_2 + Na^+ + e^- \leftrightarrow (MoS_2) - Na^+ \text{ (surface)}$$

$$MnO_2 + Na^+ + e^- \leftrightarrow (MnO_2 - Na^+) \text{ (surface)}$$

$$(MoS_2/MnO_2)_{\text{surface}} + Na^+ + e^- \leftrightarrow ((MoS_2/MnO_2) - Na^+) \text{ (surface)}$$

$$MoS_2 + Na^+ + e^- \leftrightarrow \text{Mo S} - \text{S Na (intercalation)}$$

$$MnO_2 + Na^+ + e^- \leftrightarrow \text{MnO} - \text{ONa (intercalation)}$$

$$MoS_2/MnO_2 + Na^+ + e^- \leftrightarrow (MoS_2/MnO_2)\text{Na (intercalation)}$$

For a higher concentration of MnO_2 (6 wt%), the shape of the CV curve deviates from the rectangle shape. Such leaf shape of CV curves indicates the presence of electrical double-layer capacitance (EDLC).[84–86]

3.4.2. Galvanostatic charge–discharge. The galvanostatic charge–discharge (GCD) measurements of the MoS_2 NF and MoS_2/MnO_2 NCs were taken between −0.30 V and 0.20 V at different current densities. A little deviation from the triangular and symmetrical form together with a small iR drop is observed in the GCD curves (Fig. 8(a–d)). This indicates the high reversibility of the materials and confirms the pseudocapacitive properties of the samples.[87] In the GCD curves, charging and discharging periods shorten as the density of current rises because surface adsorption and diffusion of electrolyte ions become slower into the electrode active material.[29,88,89] At low current densities, due to slow charge accumulation, access of electrolyte ions to active sites on the electrode increases through diffusion, thus providing a complete insertion/extraction reaction as well as better specific capacity.[88–90] Fig. 8(e) shows GCD curves of all samples at a current density of 0.05 A g^{-1} to compare their electrochemical performances. The specific capacitance (C_s) was estimated from the GCD curves using the formula:[29]

$$C_s = \frac{i\Delta t}{m\Delta V}$$

where m = mass of active materials, Δt = discharge time, i = discharge current, and ΔV = potential window width. Fig. 9 shows the specific capacitance of the synthesized materials as a function of current densities. At 40 mA g^{-1} current density, the specific capacitance (Fig. 9) obtained from the GCD curves was 199.12 F g^{-1}, 57.74 F g^{-1}, 48.11 F g^{-1}, for MoS_2/MnO_2 (6 wt%), MoS_2/MnO_2 (4 wt%), MoS_2/MnO_2 (2 wt%), respectively, while only 12.73 F g^{-1} for the MoS_2 NF. Here, the MoS_2/MnO_2(6 wt%) NC shows the greatest specific capacitance of all the synthesized materials.

In the GCD curve, iR drop during discharging gives the intrinsic resistance characteristics of the samples.[87] At a high discharge current density of 140 mA g^{-1}(Fig. 10), for MoS_2/MnO_2 NCs short discharge occurs because of electrical double-layer capacitance. For longer discharge electric double-layer

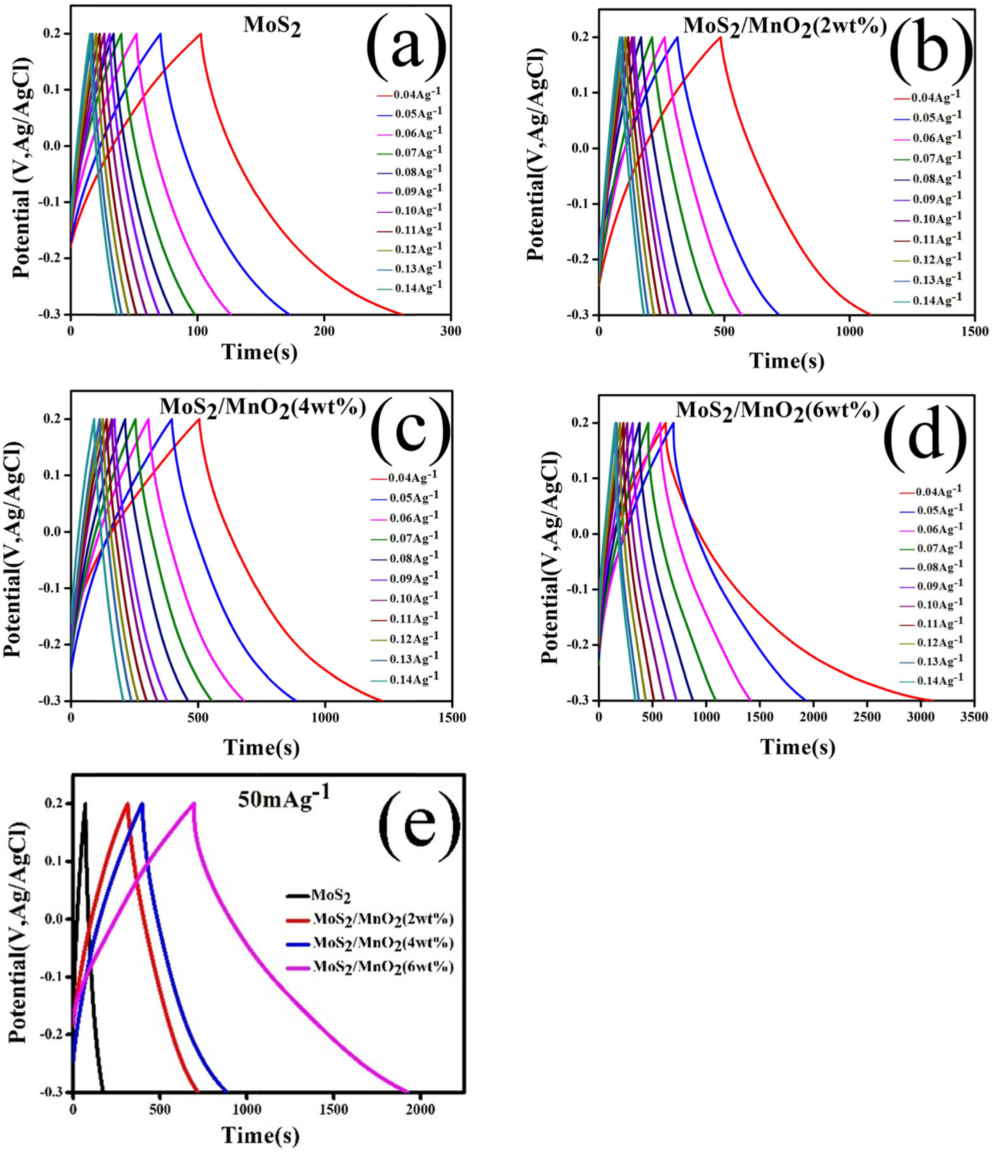

Fig. 8 (a)–(d) Galvanostatic charging–discharging curves of MoS_2 NF and MoS_2/MnO_2 NCs at various current densities. € GCD measurements at 0.05 A g^{-1}.

capacitance and faradaic capacitance are responsible.[87] The MoS_2/MnO_2 (6 wt%) nanocomposite showed the least iR drop of all the nanocomposites, suggesting less internal resistance of the active materials. During charging–discharging, energy dissipation was eliminated for lower internal resistance materials, and as a result, the energy storage performance improved.[87,91] So, to fabricate power-saving supercapacitors, the MoS_2/MnO_2 (6 wt%) nanocomposite is preferable.

The energy density (E) and power density (P) were determined from the GCD curves of the synthesized samples by using eqn (4) and (5), respectively[92]

$$E = \frac{1}{2 \times 3.6} C_s \Delta V^2 \;(\mathrm{W\,h\,kg^{-1}}) \tag{4}$$

$$P = \frac{E}{\Delta t} \times 3600 \;(\mathrm{W\,kg^{-1}}) \tag{5}$$

where ΔV = voltage window width, C_s = specific capacitance, and Δt = discharge time.

Fig. 11 illustrates the Ragone curve for the MoS_2 NF and MoS_2/MnO_2 NCs and the values are presented in the supercapacitor region.[93]

3.4.3. Electrochemical impedance spectroscopy. To investigate the capacitive and resistive properties, electrochemical impedance spectroscopy (EIS) was performed for the MoS_2 NF and MoS_2/MnO_2 NCs electrodes between 0.1 Hz and 100 kHz. Fig. 12 shows the Nyquist plots of the prepared materials. In that curve, the semicircular portion denotes the intrinsic resistance of electrodes, the middle frequency (Warburg zone) denotes the interaction between electrolyte ions and porosity of the material, and at low-frequency sudden increment in the values of impedance imaginary part can be denoted by the double-layer capacitive region.[94] The interception point in

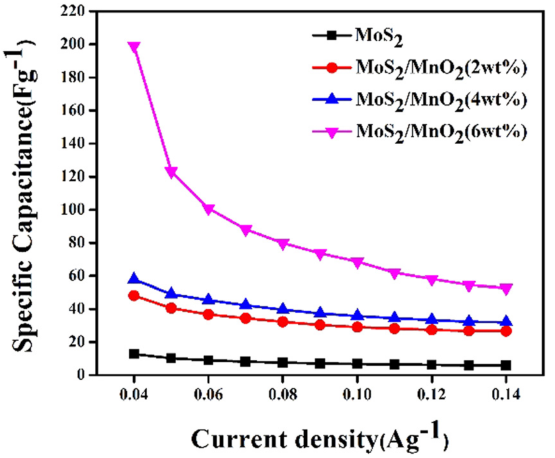

Fig. 9 Specific capacitance of MoS_2 NF and MoS_2/MnO_2 NCs at various current densities.

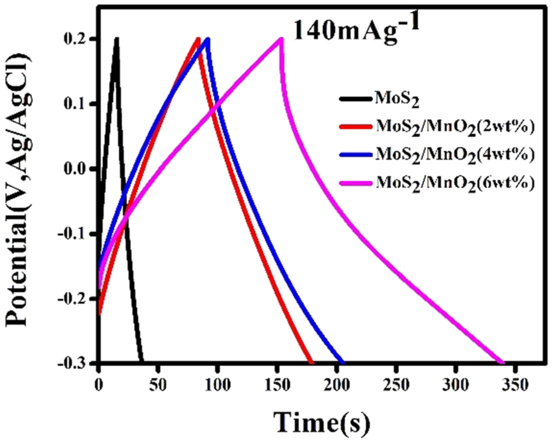

Fig. 10 GCD curves of MoS_2 NF and MoS_2/MnO_2 NCs at 140 mA g^{-1}.

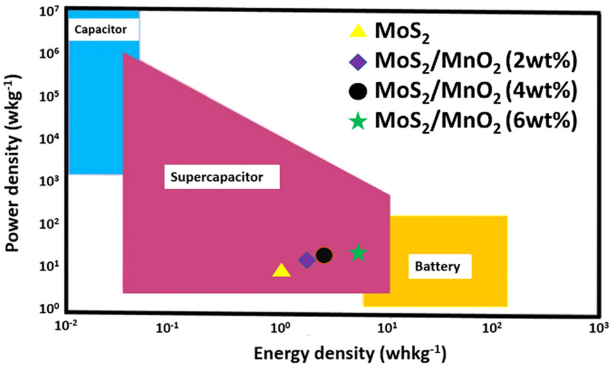

Fig. 11 Ragone curve (power density *vs.* energy density).

the high-frequency zone at the real impedance axis determines the effective series resistance value, and it can be represented as solution resistance (R_s).[95] EIS curves show that when the amount of MnO_2 increases in the MoS_2 NF, there is no interception point at the real impedance axis in the high-frequency zone. This suggests that the MoS_2 NF has more solution resistance than MoS_2/MnO_2 NCs.[29] So an increased concentration of MnO_2 in the MoS_2 NF has given better charge collection ability and faster ion transportation between electrode active materials and electrolytes.[84] The inset of Fig. 12(b) shows an equivalent circuit applied for EIS curve fitting (using ZView software). Here in the equivalent circuit W, R_{ct}, R_s, and CPE denote the Warburg impedance, charge transfer resistance, solution resistance, and constant phase element, respectively. The equivalent simulated curve is displayed in Fig. S4 (ESI†), from which all the different parameters of the equivalent circuit were determined and are listed in Table 3.

Table 3 shows that the R_{ct} (Ω) value has decreased and the CPE-T (μF) value has increased for high concentrations of MnO_2 in the MoS_2 NF indicating good electrical conductivity, high wettability, higher rate capability, increased reaction rates of the NC electrode, and better efficiency.[96,97] Quasi-semicircles and low R_{ct} are the results of double-layer capacitance as well as faradaic reactions (redox) on the electrode surface.[95] Due to enlarging interlayer distance the electrolyte gets easy access to the active material; as a result charge transfer resistance decreases when the concentration of MnO_2 increases in the MoS_2 NF.[98] Here CPE is utilized instead of a capacitor because of the compensation of the lack of uniformity in the process and represents the nonideal capacitive property, as, at the microscopic level the electrode surface is porous and rough.[98] In fact, the porosity and roughness of the surface may create a capacitance of double-layer type where the value of CPE-P in the range of 0.9 and 1 can show up as a constant phase element, and from Table 3 it can be seen that the CPE-P value of our NC samples satisfies the range. Also, when the MnO_2 concentration increases in the MoS_2 NF, the value of W (Ω) decreases. It denotes a shorter diffusion path and reduced diffusive resistance for MoS_2/MnO_2 NCs giving better electrochemical performance.[99]

From the XRD data (Table 1) the MoS_2/MnO_2 (6 wt%) nanocomposite has the highest amount of dislocation density. Improvement in the double-layer capacitive property occurs due to higher dislocation density. Increased dislocation density reduces charge transfer resistance because of the smaller phase angle, so faster electron movement occurs between the active material and the electrolyte.[98,100]

So, from the EIS data, we get that MoS_2/MnO_2 (6 wt%) NC shows better capacitive performance and this finding is compatible with CV and GCD tests.

3.4.4. Stability analysis. The stability analysis was performed for the MoS_2/MnO_2(6 wt%) sample as it provides better capacitive performance. Fig. 13(a) represents the cyclic stability plots taken up to 10 000 charge/discharge cycles at a current density of 170 mA g^{-1}. From Fig. 13(a) we observed that after 10 000 cycles retention was around 95%. The nanocomposite also gives an excellent coulombic efficiency of 106% as shown in Fig. 13(a). This superior coulombic efficiency as well as cycling stability can be attributed to the increased wettability, stability in structure, and faster ion diffusion.[101] The Nyquist

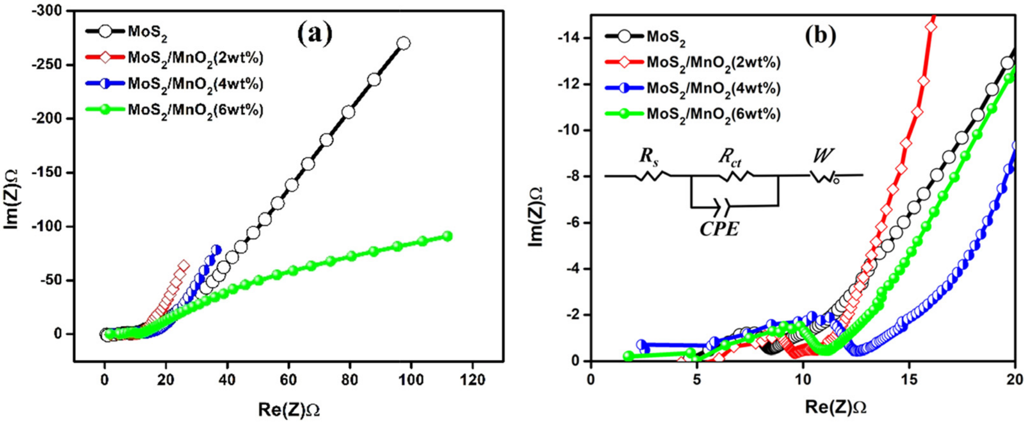

Fig. 12 (a) Nyquist curves of the synthesized samples. (b) High frequency zone Nyquist curves of the synthesized samples. The inset shows the equivalent circuit design of Randle's model.

Table 3 Fitting values of EIS for pure MoS_2 NF and MoS_2/MnO_2 NCs

Sample	R_{ct} (Ω)	CPE-T (μF)	CPE-P	W (Ω)
MoS_2	2.6	0.0835	0.99	10.16
MoS_2/MnO_2(2 wt%)	2.5	0.2520	0.95	6.55
MoS_2/MnO_2(4 wt%)	2.7	0.2600	0.98	6.39
MoS_2/MnO_2(6 wt%)	2.5	0.3309	1.00	5.93

Table 4 Fitting EIS values for the MoS_2/MnO_2 (6 wt%) nanocomposite found in the first and ten thousandth cycle

Cycle	R_{ct} (Ω)	CPE-T (μF)	CPE-P	W (Ω)
1	2.50	0.33	1.00	5.93
10 000	1.90	0.33	0.98	5.90

plots for the 1st cycle and 10 000th cycles are presented in Fig. 13(b) which demonstrates that after 10 000 cycles the radius of the semi-circular portion of the EIS spectrum becomes lower. This indicates reduced charge transfer resistance of the active materials after 10 000 cycles.[96,97] The insets of Fig. 13(b) show the fitted result and the values of the corresponding equivalent circuit components are presented in Table 4. R_{ct} and W values were found to be reduced after 10 000 cycles of operation which indicates the generation of more active sites and faster electron transport between the electrode and solution.[102,103]

3.4.5. Capacitive performance analysis of the MoS_2 NF after incorporation of the MnO_2 nanorod. For better comparison, the electrochemical performance of pure MnO_2 nanorod has been analyzed and is shown in Fig. S5 (ESI†). Fig. S6 (ESI†) exhibits the CV curve of all samples and MoS_2/MnO_2 (6 wt%) shows the highest CV area. The area of the CV curve increases with increasing the amount of MnO_2 nanorods and the largest CV area indicates better specific capacitance. The GCD curve displays a performance pattern that is similar to that. When the concentration of the MnO_2 nanorod increases in the MoS_2 NF the values of R_{ct} and W reduce. This denotes reduced resistance for charge transfer in the NCs and a shorter diffusion path of the ions in the NCs. So, the MnO_2 nanorod content affects the electrochemical performance significantly. The increased interplanar spacing, dislocation density, and surface area make the composite structure defect-rich

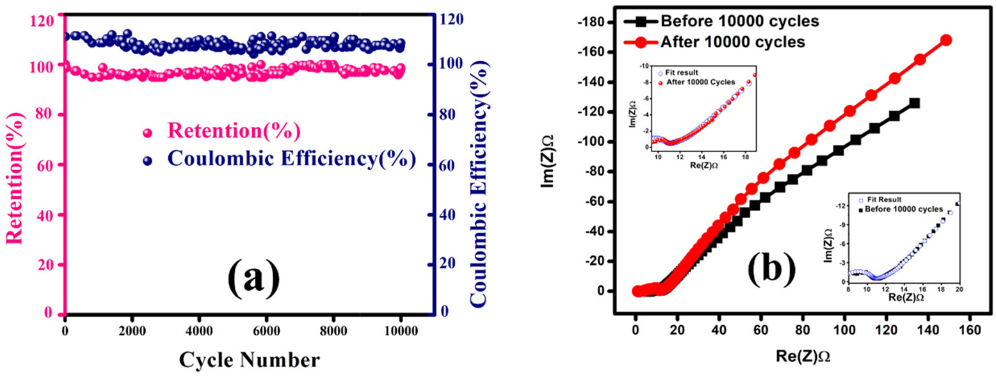

Fig. 13 (a) Coulombic efficiency and capacitive retention of the MoS_2/MnO_2 (6 wt%) nanocomposite over 10 000 cycles of charging–discharging, (b) Nyquist plots of the MoS_2/MnO_2 (6 wt%) nanocomposite before and after 10 000 cycles of charging–discharging. The insets show simulated and experimental Nyquist plots.

Table 5 Comparing the capacitance of MoS_2 based supercapacitors that have been published in the literature

Materials of electrode	Electrolyte/electrode composition (mass ratio)	Current density (A g^{-1})	Specific capacitance (F g^{-1})	Cycle number	Retained specific capacitance %	Ref.
MoS_2/Mn_3O_4	80 : 15 : 5	1	172	2000	69.3	35
MoS_2 nanospheres//Active Carbon (AC)		1	65.33			104
MoS_2NF	1 M KCl	1	168	3000	92.6	105
MoS_2-G	1 M Na_2SO_4	5	130	1000	92.3	106
MoS_2 nanowires/$NiCo_2O_4$//Active Carbon (AC)		1.5	51.7	8000	98.2	34
MoS_2-CNT	1 M Na_2SO_4	2	74	1000	80.8	24
MoS_2/MnO_2	$0.5Na_2SO_4$	.04	199.12	10 000	95	This work

and all these properties contribute to better electrochemical outcomes from the MoS_2/MnO_2 NCs. The interplanar spacing of the MoS_2 nanoflowers is increased by the incorporation of the MnO_2 nanorod, resulting in the defect-rich structure. This increased interplanar spacing might provide additional pathways for ion diffusion and electrons to the interface of the electrode while also improving the MoS_2 lattice electrical conductivity. The lower concentration of MnO_2 nanorod limits the transport of ions and electrons to the electrode surface from the electrolyte. The transport of electrons and ions from the electrolyte to the electrode surface is restricted by the lower concentration of the MnO_2 nanorod. For electrochemical reactions, MoS_2/MnO_2 (6%) offers more active sites on the surface of the electrode due to the lowest crystallite size and greater surface area among the synthesized NCs. However, as the MnO_2 amount is increased, the crystallite size decreases, and the surface area increases for chemical reactions. When the amount of MnO_2 is low, the size of the crystallite is high, limiting the number of reaction sites. Additionally, MnO_2 nanorods in the MoS_2 NF have improved the dislocation density of the produced NCs. The largest dislocation density is found in MoS_2/MnO_2 (6%) NC, which also results in an increase in capacitance value. The results and explanation above make it abundantly evident that the MoS_2/MnO_2 NCs perform better in terms of both capacitance and stability.

Table 5 presents the statistics of a MoS_2 based electrode.[24,34,104–106] Among all the reported statistics, the MoS_2/MnO_2 (6%) provides better capacitive performance. This work yields better specific capacitance with superior stability. The collaborative effect of the MoS_2 NF and MnO_2 nanorod, reduced crystallite size, defect-mediated structure, and improved electrical conductivity are responsible for this amazing outcome. So, this composite has a great deal to offer as a contender for high-performance electrode material for capacitors.

4. Conclusion

The incorporation of MnO_2 nanorods into an MoS_2 NF provides an increased surface area that is electrochemically active for charge transfer and reduces the ion diffusion length at the time of charging–discharging. The synergistic effect of a 3D-1D structure reduces the inactive volume, opening the opportunity for ions of electrolyte to access the active material. The pseudocapacitive performance alongside the electrical double-layer capacitance of the MoS_2 NF can be considerably increased by the MnO_2 nanorod. The MoS_2/MnO_2(6 wt%) nanocomposite shows a higher specific capacitance (199.12 F g^{-1} at 40 mA g^{-1}), improved capacitance retention, and cycle stability. High-performance energy storage devices can be made with this 3D-1D architectural electrode material that has exceptional electrochemical properties, enhanced stability, and coulombic efficiency.

Conflicts of interest

There are no conflicts to declare.

References

1 P. Simon and Y. Gogotsi, Materials for electrochemical capacitors, *Nat. Mater.*, 2010, 320–329, DOI: **10.1038/nmat2297**.

2 P. Y. Liu, J. J. Zhao, Z. P. Dong, Z. L. Liu and Y. Q. Wang, Interwoving polyaniline and a metal-organic framework grown in situ for enhanced supercapacitor behavior, *J. Alloys Compd.*, 2021, **854**, 157181, DOI: **10.1016/j.jallcom.2020.157181**.

3 Y. Zhao, H. Li, R. Tang, X. Wang, Y. Wu, S. Yan and Y. Zhang, Photo-assisted asymmetric supercapacitors based on dual photoelectrodes for enhanced photoelectric energy storage, *J. Mater. Chem. A*, 2023, **11**(29), 15844–15854, DOI: **10.1039/D3TA01461D**.

4 T. Zhu, J. Pan, Z. An, R. Zhe, Q. Ou and H. E. Wang, Bifunctional NiCuOx photoelectrodes to promote pseudocapacitive charge storage by in situ photocharging, *J. Mater. Chem. A*, 2022, **10**(38), 20375–20385, DOI: **10.1039/D2TA04966J**.

5 H. Lu and X. S. Zhao, Biomass-derived carbon electrode materials for supercapacitors, *Sustainable Energy Fuels*, 2017, **1**, 1265–1281, DOI: **10.1039/C7SE00099E**.

6 J. Zhang and X. S. Zhao, On the Configuration of Supercapacitors for Maximizing Electrochemical Performance, *ChemSusChem*, 2012, **5**(5), 818–841, DOI: **10.1002/cssc.201100571**.

7 K. Namsheer and C. S. Rout, Photo-powered integrated supercapacitors: a review on recent developments,

challenges and future perspectives, *J. Mater. Chem. A*, 2021, **9**(13), 8248–8278, DOI: **10.1039/D1TA00444A**.

8 C. Xu, B. Xu, Y. Gu, Z. Xiong, J. Sun and X. S. Zhao, Graphene-based electrodes for electrochemical energy storage, *Energy Environ. Sci.*, 2013, **6**(5), 1388–1414, DOI: **10.1039/C3EE23870A**.

9 Y. Zhong, X. Xia, F. Shi, J. Zhan, J. Tu and H. J. Fan, Transition metal carbides and nitrides in energy storage and conversion, *Adv. Sci.*, 2016, **3**(5), 1500286, DOI: **10.1002/advs.201500286**.

10 Y. X. Chen, K. J. Huang and K. X. Niu, Recent advances in signal amplification strategy based on oligonucleotide and nanomaterials for microRNA detection-a review, *Biosens. Bioelectron.*, 2018, **99**, 612–624, DOI: **10.1016/j.bios.2017.08.036**.

11 W. M. Huang, C. Y. Hsu and D. H. Chen, Sodium tungsten oxide nanowires-based all-solid-state flexible transparent supercapacitors with solar thermal enhanced performance, *Chem. Eng. J.*, 2022, **431**, 134086, DOI: **10.1016/j.cej.2021.134086**.

12 Y. F. Ren, Z. L. He, H. Z. Zhao and T. Zhu, Fabrication of MOF-derived mixed metal oxides with carbon residues for pseudocapacitors with long cycle life, *Rare Met.*, 2022, 1–6, DOI: **10.1007/s12598-021-01836-8**.

13 Y. H. Wang, K. J. Huang and X. Wu, Recent advances in transition-metal dichalcogenides based electrochemical biosensors: A review, *Biosens. Bioelectron.*, 2017, **97**, 305–316, DOI: **10.1016/j.bios.2017.06.011**.

14 D. Lan, Y. Chen, P. Chen, X. Chen, X. Wu, X. Pu, Y. Zeng and Z. Zhu, Mesoporous CoO nanocubes@ continuous 3D porous carbon skeleton of rose-based electrode for high-performance supercapacitor, *ACS Appl. Mater. Interfaces*, 2014, **6**(15), 11839–11845, DOI: **10.1021/am503378n**.

15 T. Wang, S. Chen, H. Pang, H. Xue and Y. Yu, MoS$_2$-based nanocomposites for electrochemical energy storage, *Adv. Sci.*, 2017, **4**(2), 1600289, DOI: **10.1002/advs.201600289**.

16 Y. Ren, T. Zhu, Y. Liu, Q. Liu and Q. Yan, Direct utilization of photoinduced charge carriers to promote electrochemical energy storage, *Small*, 2021, **17**(21), 2008047, DOI: **10.1002/smll.202008047**.

17 T. Zhu, Z. He, Z. An, R. Xu, Y. Li, R. Zhe, H. E. Wang and H. Pang, Enhancing solar energy harvest by Cu$_2$S/CuCl heteroarrays with enriched sulfur vacancies for photo-rechargeable pseudocapacitors, *Sci. China Mater.*, 2023, **66**(6), 2216–2226, DOI: **10.1007/s40843-022-2341-2**.

18 J. H. Kim, S. J. Koo, J. Y. Cheon, Y. Jung, S. Cho, D. Lee, J. W. Choi, T. Kim and M. Song, Self-powered and flexible integrated solid-state fiber-shaped energy conversion and storage based on CNT yarn with efficiency of 5.5%, *Nano Energy*, 2022, **96**, 107054, DOI: **10.1016/j.nanoen.2022.107054**.

19 W. Gu and G. Yushin, Review of nanostructured carbon materials for electrochemical capacitor applications: advantages and limitations of activated carbon, carbide-derived carbon, zeolite-templated carbon, carbon aerogels, carbon nanotubes, onion-like carbon, and graphene, *Wiley Interdiscip. Rev.: Energy Environ.*, 2014, **3**(5), 424–473.

20 P. Thounthong, V. Chunkag, P. Sethakul, S. Sikkabut, S. Pierfederici and B. Davat, Energy management of fuel cell/solar cell/supercapacitor hybrid power source, *J. Power Sources*, 2011, **196**(1), 313–324, DOI: **10.1016/j.jpowsour.2010.01.051**.

21 X. Chia, A. Y. S. Eng, A. Ambrosi, S. M. Tan and M. Pumera, Electrochemistry of nanostructured layered transition-metal dichalcogenides, *Chem. Rev.*, 2015, **115**(21), 11941–11966, DOI: **10.1021/acs.chemrev.5b00287**.

22 R. N. Bulakhe and J. J. Shim, Layer-structured nanohybrid MoS$_2$@ rGO on 3D nickel foam for high performance energy storage applications, *New J. Chem.*, 2017, **41**(4), 1473–1482, DOI: **10.1039/C6NJ02590K**.

23 N. Choudhary, M. R. Islam, N. Kang, L. Tetard, Y. Jung and S. I. Khondaker, Two-dimensional lateral heterojunction through bandgap engineering of MoS$_2$ via oxygen plasma, *J. Phys.: Condens. Matter*, 2016, **28**(36), 364002, DOI: **10.1088/0953-8984%2F28%2F36%2F364002**.

24 M. Chen, Y. Dai, J. Wang, Q. Wang, Y. Wang, X. Cheng and X. Yan, Smart combination of three-dimensional-flower-like MoS$_2$ nanospheres/interconnected carbon nanotubes for application in supercapacitor with enhanced electrochemical performance, *J. Alloys Compd.*, 2017, **696**, 900–906.

25 F. Ghasemi, M. Jalali, A. Abdollahi, S. Mohammadi, Z. Sanaee and S. Mohajerzadeh, A high performance supercapacitor based on decoration of MoS$_2$/reduced graphene oxide with NiO nanoparticles, *RSC Adv.*, 2017, **7**(83), 52772–52781, DOI: **10.1039/C7RA09060A**.

26 Y. Zhang, T. He, G. Liu, L. Zu and J. Yang, One-pot mass preparation of MoS$_2$/C aerogels for high-performance supercapacitors and lithium-ion batteries, *Nanoscale*, 2017, **9**(28), 10059–10066, DOI: **10.1039/C7NR03187D**.

27 X. Zhou, L. J. Wan and Y. G. Guo, Facile synthesis of MoS$_2$@ CMK-3 nanocomposite as an improved anode material for lithium-ion batteries, *Nanoscale*, 2012, **4**(19), 5868–5871, DOI: **10.1039/C2NR31822A**.

28 J. B. Cook, H. S. Kim, Y. Yan, J. S. Ko, S. Robbennolt, B. Dunn and S. H. Tolbert, Mesoporous MoS$_2$ as a transition metal dichalcogenide exhibiting pseudocapacitive Li and Na-ion charge storage, *Adv. Energy Mater.*, 2016, **6**(9), 1501937, DOI: **10.1002/aenm.201501937**.

29 N. Kanaujiya, N. Kumar, A. K. Srivastava, Y. Sharma and G. D. Varma, One-step synthesized mesoporous MnO$_2$@ MoS$_2$ nanocomposite for high performance energy storage devices, *J. Electroanal. Chem.*, 2018, **824**, 226–237, DOI: **10.1016/j.jelechem.2018.07.046**.

30 Y. Shen, Z. Li, Z. Cui, K. Zhang, R. Zou, F. Yang and K. Xu, Boosting the interface reaction activity and kinetics of cobalt molybdate by phosphating treatment for aqueous zinc-ion batteries with high energy density and long cycle life, *J. Mater. Chem. A*, 2020, **8**(40), 21044–21052, DOI: **10.1039/D0TA07746A**.

31 S. Ramesh, K. Karuppasamy, A. Sivasamy, H. S. Kim, H. M. Yadav and H. S. Kim, Core shell nanostructured of Co$_3$O$_4$@ RuO$_2$ assembled on nitrogen-doped graphene

sheets electrode for an efficient supercapacitor application, *J. Alloys Compd.*, 2021, **877**, 160297, DOI: 10.1016/j.jallcom.2021.160297.

32 M. Wang, H. Fei, P. Zhang and L. Yin, Hierarchically layered MoS2/Mn3O4 hybrid architectures for electrochemical supercapacitors with enhanced performance, *Electrochim. Acta*, 2016, **209**, 389–398, DOI: 10.1016/j.electacta.2016.05.078.

33 X. Liao, Y. Zhao, J. Wang, W. Yang, L. Xu, X. Tian, Y. Shuang, K. A. Owusu, M. Yan and L. Mai, MoS_2/MnO_2 heterostructured nanodevices for electrochemical energy storage, *Nano Res.*, 2018, **11**, 2083–2092.

34 S. Wen, Y. Liu, F. Zhu, R. Shao and W. Xu, Hierarchical MoS_2 nanowires/$NiCo_2O_4$ nanosheets supported on Ni foam for high-performance asymmetric supercapacitors, *Appl. Surf. Sci.*, 2018, **428**, 616e22, DOI: 10.1016/j.apsusc.2017.09.189.

35 J. Zhou, M. Guo, L. Wang, Y. Ding, Z. Zhang, Y. Tang, C. Liu and S. Luo, 1T-MoS_2 nanosheets confined among TiO_2 nanotube arrays for high performance supercapacitor, *Chem. Eng. J.*, 2019, **366**, 163–171, DOI: 10.1016/j.cej.2019.02.079.

36 Y. Zhang, T. He, G. Liu, L. Zu and J. Yang, One-pot mass preparation of MoS_2/C aerogels for high-performance supercapacitors and lithium-ion batteries, *Nanoscale*, 2017, **9**(28), 10059–10066, DOI: 10.1039/c7nr03187d.

37 N. Feng, *et al.*, A polymer-direct-intercalation strategy for MoS_2/carbon-derived heteroaerogels with ultrahigh pseudocapacitance, *Nat. Commun.*, 2019, **10**, 1372, DOI: 10.1038/s41467-019-09384-7.

38 T. Stephenson, Z. Li, B. Olsen and D. Mitlin, Lithium ion battery applications of molybdenum disulfide (MoS_2) nanocomposites, *Energy Environ. Sci.*, 2014, **7**(1), 209–231, DOI: 10.1039/c3ee42591f.

39 E. Pomerantseva and Y. Gogotsi, Two-dimensional heterostructures for energy storage, *Nat. Energy*, 2017, **2**(7), 1–6, DOI: 10.1038/nenergy.2017.89.

40 X. Zhang, Z. Lai, C. Tan and H. Zhang, Solution-processed two-dimensional MoS_2 nanosheets: preparation, hybridization, and applications, *Angew. Chem., Int. Ed.*, 2016, **55**(31), 8816–8838, DOI: 10.1002/anie.201509933.

41 X. Wang, *et al.*, High supercapacitor and adsorption behaviors of flower-like MoS2 nanostructures, *J. Mater. Chem. A*, 2014, **2**(38), 15958–15963, DOI: 10.1039/C4TA03044C.

42 Z. Wu, B. Li, Y. Xue, J. Li, Y. Zhang and F. Gao, Fabrication of defect-rich MoS_2 ultrathin nanosheets for application in lithium-ion batteries and supercapacitors, *J. Mater. Chem. A*, 2015, **3**(38), 19445–19454, DOI: 10.1039/C5TA04549E.

43 M. H. Ahmad, R. B. Alam, A. Ul-Hamid, S. F. U. Farhad and M. R. Islam, Hydrothermal synthesis of Co_3O_4 nanoparticles decorated three dimensional MoS_2 nanoflower for exceptionally stable supercapacitor electrode with improved capacitive performance, *J. Energy Storage*, 2022, **47**, 103551, DOI: 10.1016/j.est.2021.103551.

44 P. He, X. Zhao, Y. Zhang, J. Wu, N. Chen, J. Wei and T. Xu, Remove elemental mercury from simulated flue gas by flower-like MoS_2 modified with nanoparticles MnO_2, *Chem. Eng. J.*, 2021, **412**, 128588, DOI: 10.1016/j.cej.2021.128588.

45 R. Sha, A. Gopalakrishnan, K. V. Sreenivasulu, V. V. Srikanth and S. Badhulika, Template-cum-catalysis free synthesis of α-MnO_2 nanorods-hierarchical MoS_2 microspheres composite for ultra-sensitive and selective determination of nitrite, *J. Alloys Compd.*, 2019, **794**, 26–34, DOI: 10.1016/j.jallcom.2019.04.251.

46 J. G. Wang, F. Kang and B. Wei, Engineering of MnO_2-based nanocomposites for high-performance supercapacitors, *Prog. Mater. Sci.*, 2015, **74**, 51–124, DOI: 10.1039/C5TA05523G.

47 M. Huang, F. Li, F. Dong, Y. X. Zhang and L. L. Zhang, MnO_2-based nanostructures for high-performance supercapacitors, *J. Mater. Chem. A*, 2015, **3**(43), 21380–21423, DOI: 10.1039/C5TA05523G.

48 X. Duan, J. Yang, H. Gao, J. Ma, L. Jiao and W. Zheng, Controllable hydrothermal synthesis of manganese dioxide nanostructures: shape evolution, growth mechanism and electrochemical properties, *CrystEngComm*, 2012, **14**(12), 4196–4204.

49 B. H. Park and J. H. Choi, Improvement in the capacitance of a carbon electrode prepared using water-soluble polymer binder for a capacitive deionization application, *Electrochim. Acta*, 2010, **55**(8), 2888–2893, DOI: 10.1016/j.electacta.2009.12.084.

50 H. K. Park, B. S. Kong and E. S. Oh, Effect of high adhesive polyvinyl alcohol binder on the anodes of lithium ion batteries, *Electrochem. Commun.*, 2011, **13**(10), 1051–1053, DOI: 10.1016/j.elecom.2011.06.034.

51 X. Wang and Y. Li, Rational synthesis of α-MnO_2 single-crystal nanorods, *Chem. Commun.*, 2002, 764–765, DOI: 10.1039/b111723h.

52 X. Zhang, X. Huang, M. Xue, X. Ye, W. Lei, H. Tang and C. Li, Hydrothermal synthesis and characterization of 3D flower-like MoS_2 microspheres, *Mater. Lett.*, 2015, **148**, 67–70, DOI: 10.1166/nnl.2017.2321.

53 L. Hu, Y. Ren, H. Yang and Q. Xu, Fabrication of 3D hierarchical MoS_2/polyaniline and MoS_2/C architectures for lithium-ion battery applications, *ACS Appl. Mater. Interfaces*, 2014, **6**(16), 14644–14652, DOI: 10.1021/am503995s.

54 H. Fu, K. Yu, H. Li, J. Li, B. Guo, Y. Tan, C. Song and Z. Zhu, Enhanced field emission and photocatalytic performance of MoS_2 titania nanoheterojunctions via two synthetic approaches, *Dalton Trans.*, 2015, **44**(4), 1664–1672, DOI: 10.1039/C4DT03035D.

55 X. Bai, X. Tong, Y. Gao, W. Zhu, C. Fu, J. Ma, T. Tan, C. Wang, Y. Luo and H. Sun, Hierarchical multidimensional MnO_2 via hydrothermal synthesis for high performance supercapacitors, *Electrochim. Acta*, 2018, **281**, 525–533, DOI: 10.1016/j.electacta.2018.06.003.

56 Z. Wu, B. Li, Y. Xue, J. Li, Y. Zhang and F. Gao, Fabrication of defect-rich MoS_2 ultrathin nanosheets for application in lithium-ion batteries and supercapacitors, *J. Mater. Chem. A*, 2015, **3**(38), 19445–19454, DOI: 10.1039/C5TA04549E.

57 C. Chai, A. Liu, Y. Wang, Y. Lu and H. Che, A MoS_2-templated oxidation-etching strategy to synthesize hollow δ-MnO_2 nanospheres as a high-performance electrode for supercapacitor, *Ceram. Int.*, 2018, **44**(14), 16923–16930, DOI: **10.1016/j.ceramint.2018.06.132**.

58 F. Xiong, Z. Cai, L. Qu, P. Zhang, Z. Yuan, O. K. Asare, W. Xu, C. Lin and L. Mai, Three-dimensional crumpled reduced graphene oxide/MoS_2 nanoflowers: a stable anode for lithium-ion batteries, *ACS Appl. Mater. Interfaces*, 2015, 7(23), 12625–12630, DOI: **10.1021/acsami.5b02978**.

59 J. Wang, H. Zhou, M. Zhu, A. Yuan and X. Shen, Metal-organic framework-derived Co_3O_4 covered by MoS_2 nanosheets for high-performance lithium-ion batteries, *J. Alloys Compd.*, 2018, **744**, 220–227, DOI: **10.1016/j.jallcom.2018.02.086**.

60 H. Wang, Z. Lu, D. Qian, Y. Li and W. Zhang, Single-crystal α-MnO_2 nanorods: synthesis and electrochemical properties, *Nanotechnology*, 2007, **18**(11), 115616, DOI: **10.1088/0957-4484/18/11/115616**.

61 H. Song, A. Tang, G. Xu, L. Liu, Y. Pan and M. Yin, Hydrothermal synthesis and electrochemical properties of MoS_2/C nanocomposite, *Int. J. Electrochem. Sci.*, 2018, **13**, 6708–6716.

62 H. Fu, K. Yu, H. Li, J. Li, B. Guo, Y. Tan, C. Song and Z. Zhu, Enhanced field emission and photocatalytic performance of MoS_2 titania nanoheterojunctions via two synthetic approaches, *Dalton Trans.*, 2015, **44**(4), 1664–1672, DOI: **10.1039/C4DT03035D**.

63 X. Lin, X. Wang, Q. Zhou, C. Wen, S. Su, J. Xiang, P. Cheng, X. Hu, Y. Li, X. Wang and X. Gao, Magnetically recyclable MoS_2/Fe_3O_4 hybrid composite as visible light responsive photocatalyst with enhanced photocatalytic performance, *ACS Sustainable Chem. Eng.*, 2018, **7**(1), 1673–1682, DOI: **10.1021/acssuschemeng.8b05440**.

64 H. Li, K. Yu, X. Lei, B. Guo, H. Fu and Z. Zhu, Hydrothermal synthesis of novel $MoS_2/BiVO_4$ hetero-nanoflowers with enhanced photocatalytic activity and a mechanism investigation, *J. Phys. Chem. C*, 2015, **119**(39), 22681–22689, DOI: **10.1021/acs.jpcc.5b06729**.

65 G. Du, Z. Guo, S. Wang, R. Zeng, Z. Chen and H. Liu, Superior stability and high capacity of restacked molybdenum disulfide as anode material for lithium ion batteries, *Chem. Commun.*, 2010, **46**(7), 1106–1108, DOI: **10.1039/B920277C**.

66 V. Radmilovic, H. A. Gasteiger and P. N. Ross, Structure and chemical composition of a supported Pt-Ru electrocatalyst for methanol oxidation, *J. Catal.*, 1995, **154**(1), 98–106, DOI: **10.1006/jcat.1995.1151**.

67 W. S. Hummers and R. E. Offeman, Preparation of graphitic oxide, *J. Am. Chem. Soc.*, 1958, **80**(6), 1339, DOI: **10.1021/ja01539a017**.

68 X. Zhang, *et al.*, Facile synthesis of yolk–shell MoO_2 microspheres with excellent electrochemical performance as a Li-ion battery anode, *J. Mater. Chem. A*, 2013, **1**(23), 6858–6864, DOI: **10.1039/C3TA10399D**.

69 X. Zhang, *et al.*, Hydrothermal synthesis and characterization of 3D flower-like MoS_2 microspheres, *Mater. Lett.*, 2015, **148**, 67–70, DOI: **10.1016/j.matlet.2015.02.027**.

70 X. Wang, Z. Zhang, Y. Chen, Y. Qu, Y. Lai and J. Li, Morphology-controlled synthesis of MoS_2 nanostructures with different lithium storage properties, *J. Alloys Compd.*, 2014, **600**, 84–90, DOI: **10.1016/j.jallcom.2014.02.127**.

71 K. K. Paul, N. Sreekanth, R. K. Biroju, T. N. Narayanan and P. K. Giri, Solar light driven photoelectrocatalytic hydrogen evolution and dye degradation by metal-free fewlayer MoS_2 nanoflower/TiO_2(B) nanobelts heterostructure, *Sol. Energy Mater. Sol. Cells*, 2018, **185**, 364–374, DOI: **10.1016/j.solmat.2018.05.056**.

72 G. Du, Z. Guo, S. Wang, R. Zeng, Z. Chen and H. Liu, Superior stability and high capacity of restacked molybdenum disulfide as anode material for lithium ion batteries, *Chem. Commun.*, 2010, **46**(7), 1106–1108, DOI: **10.1039/b920277c**.

73 A. A. Akl and A. S. Hassanien, Microstructure and crystal imperfections of nanosized CdS_xSe_{1-x} thermally evaporated thin films, *Superlattices Microstruct.*, 2015, **85**, 67–81, DOI: **10.1016/j.spmi.2015.05.011**.

74 L. Ma, L. Xu, X. Xu, X. Zhou, J. Luo and L. Zhang, Cobalt-doped edge-rich MoS_2/nitrogenated graphene composite as an electrocatalyst for hydrogen evolution reaction, *Mater. Sci. Eng., B*, 2016, **212**, 30–38, DOI: **10.1016/j.mseb.2016.07.014**.

75 Q. Fan, A new method of calculating interplanar spacing: the position-factor method, *J. Appl. Crystallogr.*, 2012, **45**(6), 1303–1308, DOI: **10.1107/S0021889812037764**.

76 G. Tang, Y. Wang, W. Chen, H. Tang and C. Li, Hydrothermal synthesis and characterization of novel flowerlike MoS_2 hollow microspheres, *Mater. Lett.*, 2013, **100**, 15–18, DOI: **10.1016/j.matlet.2013.02.103**.

77 R. Zhou, C. Jie Han and X. Min Wang, Hierarchical MoS_2-coated three-dimensional graphene network for enhanced supercapacitor performances, *J. Power Sources*, 2017, **352**, 99–110, DOI: **10.1016/j.jpowsour.2017.03.134**.

78 X. Li, L. Zhang, X. Zang, X. Li and H. Zhu, Photo-promoted platinum nanoparticles decorated MoS_2@graphene woven fabric catalyst for efficient hydrogen generation, *ACS Appl. Mater. Interfaces*, 2016, **8**(17), 10866–10873, DOI: **10.1021/acsami.6b01903**.

79 A. Gigot, *et al.*, Mixed 1T-2H phase MoS_2/reduced graphene oxide as active electrode for enhanced supercapacitive performance, *ACS Appl. Mater. Interfaces*, 2016, **8**(48), 32842–32852, DOI: **10.1021/acsami.6b11290**.

80 S. Patil, A. Harle, S. Sathaye and K. Patil, Development of a novel method to grow mono-/few-layered MoS_2 films and MoS_2–graphene hybrid films for supercapacitor applications, *CrystEngComm*, 2014, **16**(47), 10845–10855, DOI: **10.1039/C4CE01595A**.

81 M. Huang, F. Li, F. Dong, Y. X. Zhang and L. L. Zhang, MnO_2-based nanostructures for high-performance supercapacitors, *J. Mater. Chem. A*, 2015, **3**(43), 21380–21423.

82 T. Nguyen, M. Boudard, M. J. Carmezim and M. F. Montemor, Hydrogen bubbling-induced micro/nano porous MnO_2 films prepared by electrodeposition for pseudocapacitor electrodes, *Electrochim. Acta*, 2016, **202**, 166–174.

83 X. Tao, J. Du, Y. Sun, S. Zhou, Y. Xia, H. Huang, Y. Gan, W. Zhang and X. Li, Exploring the energy storage mechanism of high performance MnO_2 electrochemical capacitor electrodes: an in situ atomic force microscopy study in aqueous electrolyte, *Adv. Funct. Mater.*, 2013, **23**(37), 4745–4751, DOI: **10.1002/adfm.201300359**.

84 A. K. Thakur, A. B. Deshmukh, R. B. Choudhary, I. Karbhal, M. Majumder and M. V. Shelke, Facile synthesis and electrochemical evaluation of PANI/CNT/MoS_2 ternary composite as an electrode material for high performance supercapacitor, *Mater. Sci. Eng., B*, 2017, **223**, 24–34, DOI: **10.1016/j.mseb.2017.05.001**.

85 J. M. Soon and K. P. Loh, Electrochemical double-layer capacitance of MoS_2 nanowall films, *Electrochem. Solid-State Lett.*, 2007, **10**(11), A250, DOI: **10.1149/1.2778851**.

86 H. Zhang, J. Wei, Y. Yan, Q. Guo, L. Xie, Z. Yang, J. He, W. Qi, Z. Cao, X. Zhao and P. Pan, Facile and scalable fabrication of MnO_2 nanocrystallines and enhanced electrochemical performance of MnO_2/MoS_2 inner heterojunction structure for supercapacitor application, *J. Power Sources*, 2020, **450**, 227616, DOI: **10.1016/j.jpowsour.2019.227616**.

87 Y. Xie and H. Du, Electrochemical capacitance of a carbon quantum dots–polypyrrole/titania nanotube hybrid, *RSC Adv.*, 2015, **5**(109), 89689–89697, DOI: **10.1039/C5RA16538E**.

88 M. Majumder, R. B. Choudhary, A. K. Thakur and I. Karbhal, Impact of rare-earth metal oxide (Eu_2O_3) on the electrochemical properties of a polypyrrole/CuO polymeric composite for supercapacitor applications, *RSC Adv.*, 2017, **7**(32), 20037–20048, DOI: **10.1039/C7RA01438D**.

89 V. K. A. Muniraj, C. K. Kamaja and M. V. Shelke, $RuO_2 \cdot nH_2O$ nanoparticles anchored on carbon nano-onions: an efficient electrode for solid state flexible electrochemical supercapacitor, *ACS Sustainable Chem. Eng.*, 2016, **4**(5), 2528–2534, DOI: **10.1021/acssuschemeng.5b01627**.

90 Y. X. Chen, W. J. Ma, K. F. Cai, X. W. Yang and C. J. Huang, In situ growth of polypyrrole onto three-dimensional tubular MoS_2 as an advanced negative electrode material for supercapacitor, *Electrochim. Acta*, 2017, **246**, 615–624.

91 C. Zhong, Y. Deng, W. Hu, J. Qiao, L. Zhang and J. Zhang, A review of electrolyte materials and compositions for electrochemical supercapacitors, *Chem. Soc. Rev.*, 2015, **44**(21), 7484–7539, DOI: **10.1039/C5CS00303B**.

92 J. Bhagwan, A. Sahoo, K. L. Yadav and Y. Sharma, Porous, one dimensional and high aspect ratio Mn_3O_4 nanofibers: fabrication and optimization for enhanced supercapacitive properties, *Electrochim. Acta*, 2015, **174**, 992–1001, DOI: **10.1016/j.electacta.2015.06.073**.

93 Y. Liu, Q. Wu, L. Liu, P. Manasa, L. Kang and F. Ran, Vanadium nitride for aqueous supercapacitors: a topic review, *J. Mater. Chem. A*, 2020, **8**(17), 8218–8233, DOI: **10.1039/d0ta01490g**.

94 C. Portet, P. L. Taberna, P. Simon and C. Laberty-Robert, Modification of Al current collector surface by sol–gel deposit for carbon–carbon supercapacitor applications, *Electrochim. Acta*, 2004, **49**(6), 905–912, DOI: **10.1016/j.electacta.2003.09.043**.

95 Y. Chen, X. Zhu, D. Yang, P. Wangyang, B. Zeng and H. Sun, A novel design of poly (3, 4-ethylenedioxythiophene): poly (styrenesulfonate)/molybdenum disulfide/poly (3, 4-ethylenedioxythiophene) nanocomposites for fabric micro-supercapacitors with favourable performances, *Electrochim. Acta*, 2019, **298**, 297–304, DOI: **10.1016/j.electacta.2018.12.083**.

96 Y. Chen, W. Ma, K. Cai, X. Yang and C. Huang, In situ growth of polypyrrole onto three-dimensional tubular MoS_2 as an advanced negative electrode material for supercapacitor, *Electrochim. Acta*, 2017, **246**, 615–624, DOI: **10.1016/j.electacta.2017.06.102**.

97 L. Ma, L. Xu, X. Xu, X. Zhou, J. Luo and L. Zhang, Cobalt-doped edge-rich MoS_2/nitrogenated graphene composite as an electrocatalyst for hydrogen evolution reaction, *Mater. Sci. Eng., B*, 2016, **212**, 30–38.

98 E. Rafiee, M. Farzam, M. A. Golozar and A. Ashrafi, An investigation on dislocation density in cold-rolled copper using electrochemical impedance spectroscopy, *Int. Scholarly Res. Not.*, 2013, **2013**, 921825, DOI: **10.1155/2013/921825**.

99 C. Lamiel and J. J. Shim, Hierarchical mesoporous graphene@Ni-Co-S arrays on nickel foam for high-performance supercapacitors, *Electrochim. Acta*, 2015, **161**, 351–357, DOI: **10.1016/j.matlet.2016.02.017**.

100 Y. Jia, Y. Lin, Y. Ma and W. Shi, Hierarchical MnS_2-MoS_2 nanotubes with efficient electrochemical performance for energy storage, *Mater. Des.*, 2018, **160**, 1071–1079, DOI: **10.1016/j.matdes.2018.10.031**.

101 D. Li, *et al.*, Transparent 1T-MoS_2 nanofilm robustly anchored on substrate by layer-by-layer self-assembly and its ultra-high cycling stability as supercapacitors, *Nanotechnology*, 2017, **28**(39), 395401, DOI: **10.1088/1361-6528/aa7ee3**.

102 M. R. Islam, S. N. S. Pias, R. B. Alam and S. I. Khondaker, Enhanced electrochemical performance of solution-processed single-wall carbon nanotube reinforced polyvinyl alcohol nanocomposite synthesized via solution-cast method, *Nano Exp.*, 2020, **1**(3), 030013, DOI: **10.1088/2632-959X/abc050**.

103 M. R. Islam and S. I. Mollik, Enhanced electrochemical performance of flexible and eco-friendly starch/graphene oxide nanocomposite, *Heliyon*, 2020, **6**(10), e05292, DOI: **10.1016/j.heliyon.2020.e05292**.

104 Y.-P. Gao, K.-J. Huang, X. Wu, Z.-Q. Hou and Y.-Y. Liu, MoS2 nanosheets assembling three-dimensional nanospheres for enhanced-performance supercapacitor, *J. Alloys Compd.*, 2018, **741**, 174e81, DOI: **10.1016/j.jallcom.2018.01.110**.

105 X. Wang, J. Ding, S. Yao, X. Wu, Q. Feng, Z. Wang and B. Geng, High supercapacitor and adsorption behaviors of flower-like MoS_2 nanostructures, *J. Mater. Chem. A*, 2014, **2**(38), 15958–15963.

106 K.-J. Huang, L. Wang, Y.-J. Liu, Y.-M. Liu, H.-B. Wang and T. Gan, *et al.*, Layered MoS2egraphene composites for supercapacitor applications with enhanced capacitive performance, *Int. J. Hydrogen Energy*, 2013, **38**, 14027e34, DOI: **10.1016/J.IJHYDENE.2013.08.112**.